JOURNAL OF GEOPHYSICAL RESEARCH, VOL. 106, NO. A4, PAGES 5945–5956, APRIL 1, 2001

# Energy characteristics of auroral electron precipitation: A comparison of substorms and pressure pulse related auroral activity

D. Chua[1], G. Parks[1], M. Brittnacher[1], W. Peria[1], G. Germany[2], J. Spann[3], and C. Carlson[4]

**Abstract.** The Polar Ultraviolet Imager (UVI) observes auroral responses to incident solar wind pressure pulses and interplanetary shocks such as those associated with coronal mass ejections (CMEs). The arrival of a CME pressure pulse at the front of the magnetosphere results in highly disturbed geomagnetic conditions and a substantial increase in both dayside and nightside auroral precipitation. Our observations show a simultaneous brightening over broad areas of the dayside and nightside aurora in response to a pressure pulse, indicating that more magnetospheric regions participate as sources for auroral precipitation than during isolated substorms. We estimate the average energies of incident auroral electrons using Polar UVI images and compare the precipitation energies during pressure pulse associated events with those during isolated auroral substorms. Electron precipitation during substorms has average energies greater than 10 keV and is structured both in local time and magnetic latitude. For auroral intensifications following the arrival of a pressure pulse or interplanetary shock, electron precipitation is less spatially structured and has greater flux of lower-energy electrons ($E_{\rm ave} \leq 7$ keV) than during isolated substorm onsets. The average energies of the precipitating electrons inferred from UVI are consistent with those measured in situ by the Fast Auroral Snapshot (FAST) spacecraft. These observations quantify the differences between global and local auroral precipitation processes and will provide a valuable experimental check for models of sudden storm commencements and magnetospheric response to perturbations in the solar wind.

## 1. Introduction

The interaction of the magnetosphere with shocks in the solar wind, particularly those associated with interplanetary pressure pulses (IPPs) and coronal mass ejections (CMEs), is receiving considerable attention in light of current efforts to improve space weather forecasting and to increase our understanding of the Sun-Earth environment. End-to-end monitoring of such events by the fleet of International Solar-Terrestrial Physics (ISTP) spacecraft and complementary ground-based observations affords unprecedented opportunities to study the magnetospheric response to strong disturbances in the solar wind as demonstrated by the well studied January 6-11, 1997, magnetic cloud event [*Fox et al.*, 1998, and references therein]. Interplanetary pressure pulses are identified as transient enhancements in solar wind ion density, sometimes carried by flow velocities as high as 1000 km $s^{-1}$ [*Kahler*, 1992]. The causal relationship between solar wind disturbances and geomagnetic storms has been demonstrated by *Gonzales and Tsurutani* [1987], who show a strong association between sudden storm commencements (SSCs) and the presence of density enhancements and large amplitude interplanetary magnetic fields (IMF) in the solar wind. *Brueckner et al.* [1998] report that geomagnetic storms consistently follow CMEs and their associated shocks observed directly by the Solar and Heliospheric Observatory (SOHO) spacecraft. These observations underscore the strong energy coupling between the magnetosphere and solar wind during CME-driven interplanetary pressure pulses and shocks.

Studies of magnetospheric plasma dynamics following the passage of CMEs and magnetic clouds have predominantly focused on more energetic populations such as the acceleration of relativistic electrons in the outer magnetosphere [*Baker et al.*, 1998] and their transport to lower $L$ shells [*Li et al.*, 1998]. Our knowledge of how

[1]Geophysics Program, University of Washington, Seattle.
[2]Center for Space Plasma, Aeronomic, and Astrophysics Research, University of Alabama in Huntsville.
[3]NASA Headquarters, Washington, D. C..
[4]Space Sciences Laboratory, University of California, Berkeley.



Paper number 2000JA003027.
0148-0227/01/2000JA003027$09.00

auroral and ionospheric particle populations respond to CME-type disturbances is more limited. Recent case studies using auroral imaging by the Polar Ultraviolet Imager (UVI) [*Torr et al.*, 1995] have generally shown that the auroral response to incident pressure pulses occurs much more rapidly than convection timescales [*Spann et al.*, 1998; *Zhou and Tsurutani*, 1999a; *Brittnacher et al.*, 2000]. These observations have raised several key questions regarding the source regions of auroral precipitation during CME-magnetosphere interactions, as well as what processes may be operative during these events. How much direct access solar wind particles have to the auroral zone during CME passages is also unclear.

Understanding the complex dynamics governing the response of the magnetosphere-ionosphere system to interplanetary pressure pulses is important because their interaction involves fundamental mechanisms of mass and energy transport from the solar wind into the magnetosphere. Moreover, *Zhou and Tsurutani* [1999b] have suggested that interplanetary pressure pulses may play an important role in triggering auroral substorms. Previous descriptions of the auroral response to the arrival of interplanetary pressure pulses and CMEs have been largely qualitative. We will extend previous studies of auroral morphology following pressure pulse and CME arrivals by using Polar UVI images to estimate the incident energy flux and mean energies of the electron precipitation during these events. We first illustrate the morphological differences between isolated substorms and pressure pulse/CME related auroral intensifications. The energy characteristics of the electron precipitation following the arrival of an interplanetary pressure pulse (shock) are compared with those for an isolated auroral substorm. Through this comparison, we demonstrate how isolated auroral substorms and pressure pulse related intensifications represent different processes in the magnetosphere-ionosphere system.

## 2. Method

The use of multispectral auroral imaging as a means of remote sensing ionospheric parameters and energy characteristics of auroral precipitation has been developed extensively in previous work [*Strickland et al.*, 1983; *Rees and Lummerzheim*, 1989; *Germany et al.*, 1994a, 1994b, 1998; *Lummerzheim et al.*, 1991]. These techniques typically measure the brightness of auroral emissions at two different wavelengths or passbands: one which experiences varying degrees of atmospheric extinction (as a function of the energy of the precipitating particle causing the emission) and another for which attenuation by the atmosphere is negligible. The ratio of these intensities provides an energy-dependent measurement which can be input to some electron transport model to yield estimates of auroral electron energy characteristics.

The application of this technique to images obtained by Polar UVI is described in detail by *Germany et al.* [1994a, 1994b; 1998] and is only summarized briefly here. UVI images the Lyman-Birge-Hopfield (LBH) emissions caused by electron impact excitation of molecular $N_2$ in two passbands. The LBH-long (LBHl) filter is centered around 170 nm where the LBH emissions are less affected by $O_2$ absorption. Electron transport modeling performed by *Germany et al.* [1994a, 1994b] allows the incident electron energy flux to be estimated directly from the photon flux observed in the LBHl filter. The LBH-short (LBHs) filter is centered near 150 nm, where the LBH emissions are strongly affected by Schumann-Runge $O_2$ absorption. Intensities observed through the LBHs filter are sensitive to the energy of the incident electrons causing the emissions: photons originating lower in the atmosphere, created by higher-energy electrons, must pass through a thicker column of $O_2$ and suffer greater extinction before reaching the UVI detector. Thus the photon flux measured in the LBHs filter depends on the energy spectrum of the incident electrons, which we describe by their average energy. The average energy of the incident electrons is computed from the LBHl:LBHs ratio rather than just the LBHs photon flux alone in order to normalize for varying levels of incident energy flux. For any given energy distribution, *f(E)*, the mean energy is defined as

$$E_{\text{ave}} = \frac{\int E\, f(E)\, dE}{\int f(E)\, dE}. \tag{1}$$

The average energies estimated from the UVI images are computed on the basis of a Gaussian energy distribution. Maxwellian distributions have also been used for this purpose [e.g., *Strickland et al.*, 1989]. However, *Germany et al.* [1994a, 1994b] demonstrated that the modeled column-integrated LBH emission intensities varied by less than 20% between input Gaussian and Maxwellian electron energy distributions. For the choice of energy distribution to be significant, the errors in the UVI data would have to be much less than 20%, which is generally not the case. For UVI the uncertainties in the mean energy estimation are typically 30% or greater. Uncertainties in the UVI-estimated energy flux are determined by Poisson statistics. Because the photon flux measured in the LBHl filter has a small contribution from emissions in the LBHs passband as well, the LBHl photon flux is weakly energy dependent. For incident electrons with energies between 2 and 15 keV this energy dependence is small and assumed to be negligible. Our analysis of precipitating electron energy characteristics is applied in this energy range.

Each pixel in the LBHl and LBHs images is mapped into 1.0° magnetic latitude (MLAT) × 0.5 hour magnetic local time (MLT) bins over all local times and magnetic latitudes between 60° and 90° using Apex coordinates [*Richmond*, 1995]. For each MLT-MLAT bin we compute the average photon flux (photons $cm^{-2}\ s^{-1}$) observed through the LBHl and LBHs filters in addition to the incident energy flux inferred from the LBHl images. This binning is used to overcome not having

a one-to-one spatial correspondence between the pixels in the LBHl and LBHs images which are acquired at different times. The UVI images used in this study are obtained in the following sequence: LBHl 18.4-s integration, LBHl 36.8-s integration, LBHs 18.4-s integration, and LBHs 36.8-s integration. The 36.8-s LBHl images are used to estimate the incident energy flux as shown in Plate 1a and Plate 2a. To improve the signal-to-noise ratio for computing the average energies, the separate 18.4-s and 36.8-s frames for each filter are summed to form LBHl and LBHs images with effective integration periods of 55.2 s. In this mode the time resolution between images taken with the same filter and integration period is 3 min. The time label on each image references the beginning of the integration.

Rapid increases in incident energy flux will produce high counts in the LBHl images while the preceding LBHs images with which the LBHl:LBHs ratio can be computed may not reflect this increase in activity. This scenario is prevalent during auroral intensifications and can result in an overestimate of the precipitating electron mean energy. To minimize this effect on the $E_{\text{ave}}$ computation, interpolated values of LBHl (LBHs) photon flux are computed for the time intervals in which LBHs (LBHl) data are taken. Measured and interpolated intensities are combined to form a time series of LBHl and LBHs photon fluxes in each MLT-MLAT bin from which the LBHl:LBHs ratios and mean energies are computed. Thus $E_{\text{ave}}$ values are computed at a time resolution of 1.5 min. Average energy values in MLAT-MLT bins where the photon flux in either the LBHl or LBHs filter is less than 4 photons $\text{cm}^{-2}$ $\text{s}^{-1}$ are rejected. This flux threshold represents the value above which the counts in the UVI detector become statistically significant.

The airglow contribution to the UVI images is removed by a technique similar to that described by *Lummerzheim et al.* [1997]. Pixels in the dayside portion of an image affected by airglow are binned according to solar zenith angle, excluding the auroral contribution. An empirical dayglow model is then constructed, and the airglow is subtracted from each UVI image. We also construct keograms from the UVI images (Plate 1c and Plate 2c) which show the average incident energy flux (odd-numbered panels) and mean energy (even-numbered panels) within a specified local time region as a function of magnetic latitude and UT.

## 3. Observations

There are considerable variations between auroral intensifications in terms of morphology and magnitude. Our definition of an "isolated auroral substorm" includes those events that generally conform to the *Akasofu* [1964] phenomenological auroral substorm description during which only one optical signature of substorm onset is observed (auroral brightening and the poleward motion of midnight sector auroral oval). The classical auroral substorm description provides the context within which we compare pressure pulse related auroral intensifications. For this study we selected events for which UVI simultaneously observes both the dayside and nightside regions of the auroral oval. We describe an event which occurs on December 18, 1996 (961218), as an example of an isolated substorm. The UVI observations following the arrival of an interplanetary shock on August 26, 1998 (980826), are selected to illustrate the auroral response to such solar wind disturbances. These two events are representative cases which illustrate the differences between the two types of auroral activity described in this study. A statistical analysis of a larger number of isolated substorms and pressure pulse related events is in progress and will be reported at a later time.

### 3.1. Energy Flux and Morphology

The morphological features of a typical isolated auroral substorm are illustrated in the UVI images and auroral energy flux keograms shown in Plate 1 for an event that occured on December 18, 1996. The energy flux keograms for this event are shown for the following local time sectors: evening (2000-2200 MLT), premidnight (2200-0000 MLT), postmidnight (0000-0200 MLT), and dawn (0500-0700 MLT). The gap in the keograms between 0553 and 0556 UT is due to a shift of the platform on which the UVI instrument is mounted on the Polar spacecraft. The onset of this isolated substorm occurs between 0530:36 and 0533:40 UT and is seen in the 0533:04 UT LBHl image as an enhancement in incident energy flux from 2.7 ± 1.6 to 19.2 ± 4.4 ergs $\text{cm}^{-2}$ $\text{s}^{-1}$ within a limited local time region between 2300-2330 MLT. Energy fluxes in the dawn (0200-0700 MLT) and dusk (1500-2000 MLT) sectors do not change significantly during the substorm onset and remain below 3.1 ± 1.8 ergs $\text{cm}^{-2}$ $\text{s}^{-1}$ until after 0536:08 UT (Plate 1a). Throughout this isolated substorm we observe very little auroral activity in the dayside oval between 0900-1500 MLT where incident electron energy flux remains below 1.5 ± 1.2 ergs $\text{cm}^{-2}$ $\text{s}^{-1}$.

The sequence of UVI images in Plate 1a shows the spatial development of the substorm expansion phase which is marked by the poleward enhancement of auroral precipitation over an increasingly wider local time region around the onset location between 0533 and 0551 UT. In the postmidnight sector the substorm expansion region is observed to reach 0300 MLT by 0542:16 UT, where the mean energy flux is 12.6 ± 3.5 ergs $\text{cm}^{-2}$ $\text{s}^{-1}$. The westward surge of the substorm expansion region reaches 1900 MLT by 0551:28 UT. From the UVI images between 0536:08 and 0551:28 UT we estimate the velocity of the westward surge to be 1.1 km $\text{s}^{-1}$ along the auroral oval, which is consistent with previous optical observations [*Akasofu et al.*, 1969]. In the 1900-2100 MLT region a peak energy flux of 36.3 ± 6.0 ergs $\text{cm}^{-2}$ $\text{s}^{-1}$ is observed near 74.5° MLAT. The westernmost region of the substorm expansion continues to have the highest levels of incident energy flux throughout this event, as

can be seen in the 0551:28 UT and 0603:44 UT images (Plate 1a).

The latitudinal enhancement of auroral activity following the substorm onset is more readily seen in the midnight sector keograms for this event (Plate 1c, panels 3 and 5) which show elevated energy fluxes at increasingly higher magnetic latitudes between 0533 and 0551 UT. The poleward boundary of the midnight sector auroral oval is identified by selecting the magnetic latitude at which the incident energy flux falls below 1.0 ergs $cm^{-2}$ $s^{-1}$, which corresponds to the lower limit of statistically significant counts in the UVI images. The value of this threshold is also empirically determined on the basis that most high-latitude polar cap precipitation, with the exception of such discrete structures as transpolar arcs, is observed with energy fluxes well below 1.0 ergs $cm^{-2}$ $s^{-1}$ [*Brittnacher et al.*, 1999]. Using this energy flux criterion, we observe the poleward boundary of the oval in both the premidnight (2200-0000 MLT) and postmidnight (0000-0200 MLT) sectors to shift from 73° MLAT prior to the onset (0530 UT) to 86° MLAT when it reaches its most poleward location (0551 UT) at a rate of 0.5° MLAT per minute. This is shown in Plate 1c (panels 3 and 5) by the red traces overlaid on the premidnight and postmidnight sector keograms. The poleward boundary of the auroral oval can also be identified by choosing the latitude where the incident energy flux falls off by $e^{-1}$ of its peak value in that local time sector. The $e$-folding criterion yields a slower poleward expansion rate of 0.3° MLAT per minute between 70° and 78° MLAT, as shown by the white traces in panels 3 and 5. A poleward excursion of the auroral oval is not observed in the dawn and dusk sectors (Plate 1c, panels 5 and 7) during the expansion phase of this substorm.

By 0603 UT a decrease in the incident energy flux is observed over most of the substorm expansion except within its westernmost region between 1900 and 2100 MLT, where a mean energy flux of 20.4 ± 4.5 ergs $cm^{-2}$ $s^{-1}$ persists (Plate 1a). As the substorm moves into the early recovery phase at this time, the decrease in energy flux within the midnight sector after 0603 UT is accompanied by an equatorward retreat of the poleward boundary between 2300-0100 MLT as seen in energy flux keograms for this local time region (Plate 1c, panels 1 and 3) between 0603 and 0613 UT. During this time interval, we observe a broadening of the dawn sector auroral oval, predominately toward lower latitudes (Plate 1c, panel 5). No significant motion of the dusk sector auroral oval is observed throughout this isolated auroral substorm.

On August 26, 1998, at ~ 0640 UT the Wind spacecraft encountered a CME-driven interplanetary shock at its upstream location of ($X_{GSE}$ = 117.0 $R_E$, $Y_{GSE}$ = -21.6 $R_E$, $Z_{GSE}$ = -7.6 $R_E$). At this time, the dynamic pressure jumped from 2 nPa to above 10 nPa with a fourfold increase in proton density downstream of the shock (not shown). Further details of the in situ Wind observations of this interplanetary shock are given by *Bale et al.* [1999]. The Polar UVI observations of the auroral response to this interplanetary shock are given in Plate 2. The keograms derived from the UVI images for this event are shown for the midnight (2300-0100), dawn (0500-0700 MLT), noon (1100-1300 MLT), and dusk (1700-1900 MLT) magnetic local time sectors. The data drop-out in the keograms between 0750 and 0810 UT is caused by the auroral oval moving out of the UVI field of view prior to a shift in the UVI viewing orientation.

Prior to the arrival of the interplanetary shock, we observe preexisting activity in the 1800-2400 MLT sector with a mean energy flux of 5.3 ± 2.3 ergs $cm^{-2}$ $s^{-1}$ (Plate 2a, 0650:52 UT image). This is the remnant of a previous auroral intensification that occurred between 0450 and 0600 UT (not shown). Auroral activity throughout the dawn flank and dayside regions is low between 0622-0650 UT. During this period the mean energy flux between 70° and 75° MLAT in the dawn and dusk keograms (Plate 2c, panels 3 and 7) is comparable at ~ 2.6 ± 1.6 ergs $cm^{-2}$ $s^{-1}$. The average energy flux in the noon sector (1100-1300 MLT) is 1.7 ±1.3 ergs $cm^{-2}$ $s^{-1}$ prior to the pressure pulse arrival. There is no significant latitudinal motion of the auroral oval at all local times between 0622 and 0650 UT. A localized region of higher auroral activity is observed at 0650 UT near 1500 MLT with a mean energy flux of ~ 2.9 ± 1.7 ergs $cm^{-2}$ $s^{-1}$. This region has been identified by previous studies as one of two maxima of dayside auroral activity [e.g., *Cogger et al.*, 1977; *Liou et al.*, 1997, 1999].

In the following we estimate the time delay between the arrival of the CME-driven, interplanetary shock at the dayside magnetosphere and the global auroral intensification observed near 0653 UT. We estimate an equatorial magnetopause standoff distance of ~ 7.8 ± 0.2 $R_E$ based on the solar wind conditions measured prior to the shock arrival by the Wind spacecraft (not shown). *Bale et al.* [1999] estimate a shock velocity of 1300 km $s^{-1}$ and a shock normal direction of ($\hat{x}_{GSE} \approx$ -0.93, $\hat{y}_{GSE} \approx$ -0.09, $\hat{z}_{GSE} \approx 0.36$). Assuming these properties, we estimate the transit time of the interplanetary shock between the Wind spacecraft location and the dayside magnetopause at the stand-off distance given above to be ~ 9 ± 1 min. This gives an arrival time of the pressure pulse at the magnetosphere near 0648-0650 UT. The initial brightening of both dayside and nightside auroral zones near 0653 UT occurred no later than 5 min following the arrival of the solar wind pressure pulse at the dayside magnetopause. The auroral response to the incident pressure pulse occurred on Alfvén wave timescales rather than convection timescales (tens of minutes) in the magnetosphere.

The spatial and temporal evolution of auroral activity in response to a solar wind pressure pulse is distinct from that observed during an isolated substorm. The most distinguishing feature is the latitudinal expansion

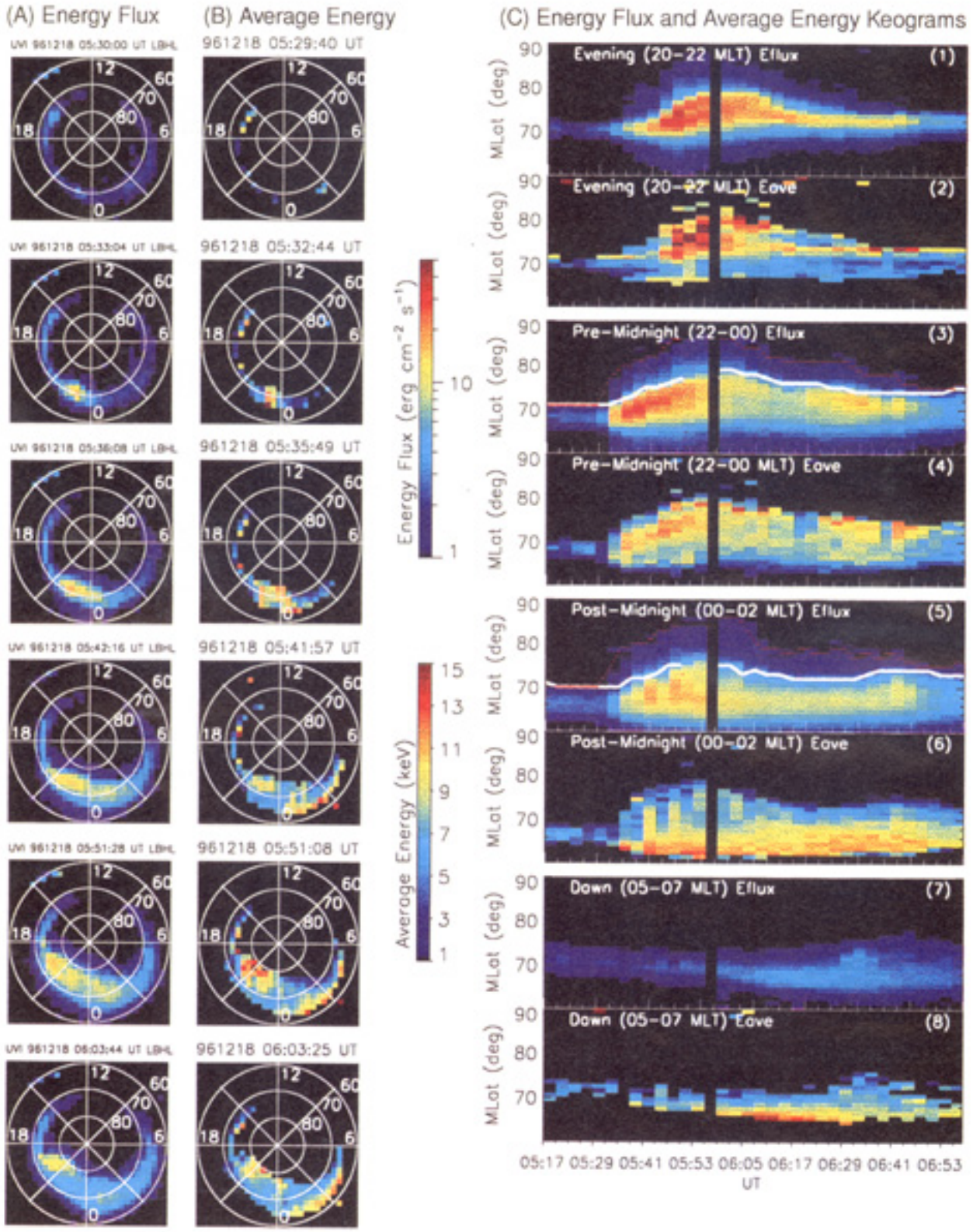


**Plate 1.** Polar Ultraviolet Imager (UVI) observations for the isolated substorm on December 18, 1996: UVI Lyman-Birge-Hopfield-long (LBHl) images scaled in units of incident auroral energy flux (ergs cm$^{-2}$ s$^{-1}$). $E_{ave}$ maps in units of keV derived from the LBHl:Lyman-Birge-Hopfield-short (LBHs) image ratio. Auroral keograms for energy flux (odd-numbered panels) and mean energy (even-numbered panels). The red traces shown for the premidnight (Plate 1c, panel 3) and the postmidnight (Plate 1c, panel 5) energy flux keograms indicate the poleward boundary of the auroral oval at these local times as determined by the 1.0 ergs cm$^{-2}$ s$^{-1}$ threshold. The white traces mark the midnight sector poleward boundaries determined by the ($e$-folding) criterion.

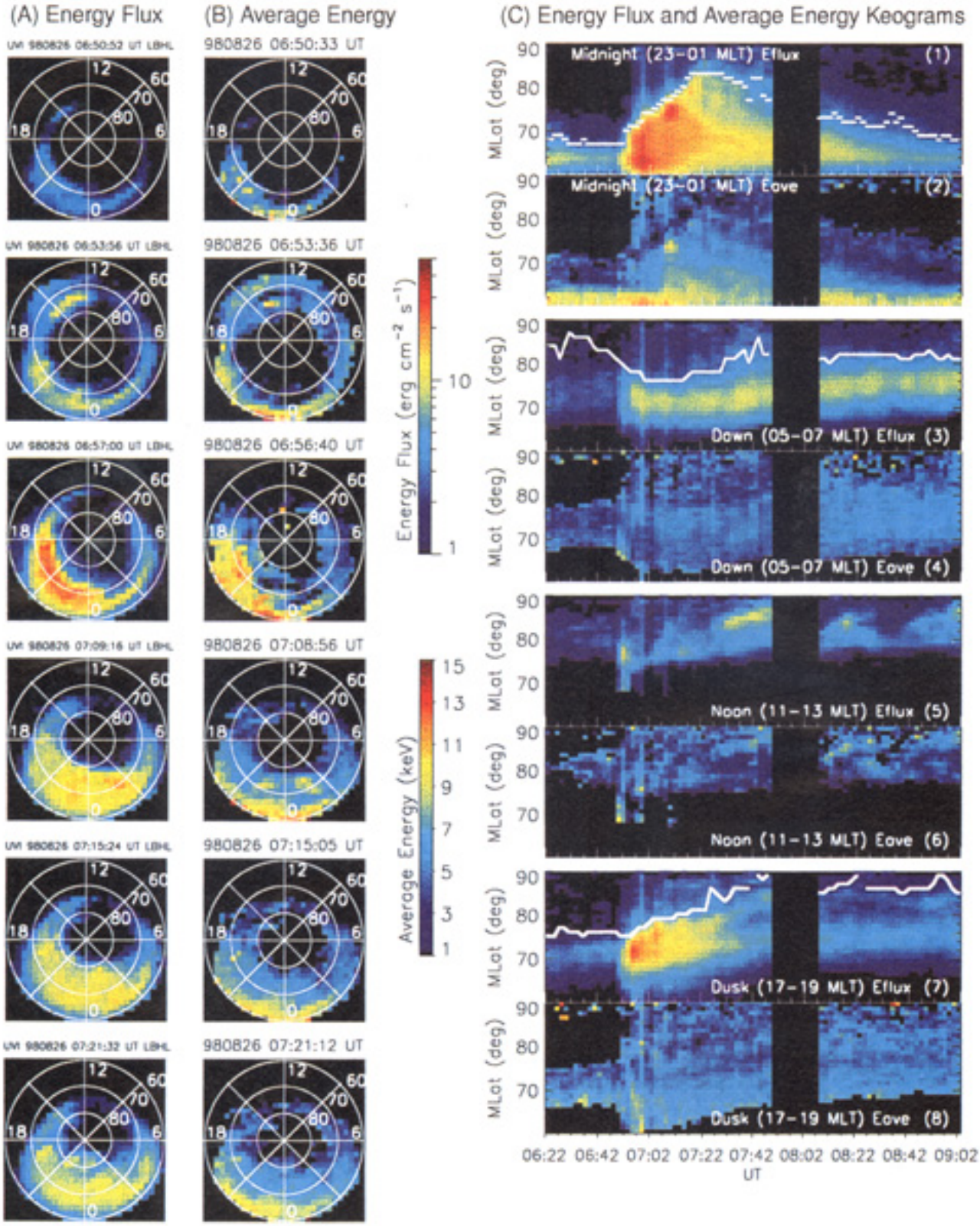


**Plate 2.** (a-c) UVI observations of the auroral oval in response to the coronal mass ejection (CME)-driven interplanetary pressure pulse on August 26, 1998. The format is the same as that for Plate 1. The white trace on the midnight sector energy flux keogram indicates the poleward boundary of the auroral oval in this local time sector as determined by the $e$-folding criterion.

of the auroral oval and enhancement of incident energy flux at all local times rather than within a limited longitudinal region as in the isolated substorm described above. This can be seen by comparing the 0650:52 and 0653:36 UT images in Plate 2a which show a global enhancement in auroral activity. At the location of the initial dayside auroral brightening between 1200-1500 MLT, incident energy flux increased by a factor of 5 from the previous mean value of 1.7 ± 1.3 to 8.8 ± 2.9 ergs $cm^{-2}$ $s^{-1}$ (Plate 2a, 0653:56 UT image). Another feature to note at this time is the transient brightening equatorward of the dayside auroral oval between 0600 and 1800 MLT at magnetic latitudes less than 70°. The energy flux in this region equatorward of the dayside oval has a maximum of 15.8 ± 4.0 ergs $cm^{-2}$ $s^{-1}$ near 1500 MLT and 66° MLAT (Plate 2a, 0653:52 UT image). This feature persists equatorward of the postnoon auroral oval with incident energy flux of 7.3 ± 2.7 ergs $cm^{-2}$ $s^{-1}$ until after the 0657:00 UT image. The average energy flux in the premidnight sector between 1800-2300 MLT increases to 9.6 ± 3.1 ergs $cm^{-2}$ $s^{-1}$ between the 0650:52 and 0653:56 UT images (Plate 2a). This enhancement in incident energy flux in the premidnight sector is greater than three standard deviations above the mean energy flux measured in the preexisting activity in this region prior to the arrival of the pressure pulse.

The global expansion of the auroral oval following the interplanetary shock arrival is further demonstrated by the energy flux keograms shown in Plate 2c (odd-numbered panels). Near 0653 UT we observe an abrupt broadening of the auroral oval that is most pronounced in the midnight (panel 1) and dusk (panel 7) local time sectors. The energy flux increases by a factor of 6 to 16.6 ± 2.6 ergs $cm^{-2}$ $s^{-1}$ in the dusk sector and 25.3 ± 5.0 ergs $cm^{-2}$ $s^{-1}$ in the midnight sector after the shock arrival. The expansion of activity over a wider latitude range at 0653 UT is also evident in the dawn sector (panel 3) keogram although the increase in average energy flux is only a factor of 3 from 2.6 ± 1.6 to 7.7 ± 0.8 ergs $cm^{-2}$ $s^{-1}$. In the noon sector (panel 5) the oval transiently expands equatorward between 0653 and 0703 UT with a fourfold enhancement in energy flux to 6.4 ± 1.3 ergs $cm^{-2}$ $s^{-1}$ between 70° and 80° MLAT.

In contrast to the isolated substorm, the precipitating electron energy flux at high latitudes and in the polar cap is significantly greater during this pressure pulse related event. The UVI images between 0653:56 and 0657:00 UT show that the increase in auroral precipitation at high latitudes initially occurs in the dusk and premidnight auroral oval, expanding eastward toward the dawn sector, as well as broadening in latitude at all local times by 0709:16 UT (Plate 2a). No westward surge-like feature is observed during this pressure pulse related intensification as is typically seen during substorms. The energy flux criterion used to identify the poleward boundary of the auroral oval for the December 18, 1996, event fails in this case at all local times because the energy flux within the polar cap (normally considered the region poleward of the auroral oval where flux tubes are thought to be open to the solar wind) exceeds the 1.0 ergs $cm^{-2}$ $s^{-1}$ threshold in both the dayside and nightside auroral zones after 0653 UT. In this case, the $e$-folding criterion is used to describe the poleward motion of the midnight sector oval, which moves from roughly 72° MLAT to 83° MLAT between 0653 and 0712 UT as shown by the white trace overlaid on the keogram in panel 1 of Plate 2c. The rate of poleward expansion of the midnight sector oval is twice as fast (0.6° MLAT per minute) as that during the isolated substorm by the same $e$-folding criterion. The response of the auroral oval in the dusk (1700-1900 MLT) and dawn (0500-0700 MLT) sectors following the pressure pulse arrival is asymmetric. Between 0653 and 0722 UT, the $e$-folding boundary in the dusk sector moves poleward at a steady rate of ~ 0.3° per minute. In contrast the auroral oval in the dawn sector is observed to shift slightly equatorward from 83° MLAT to 77° MLAT following the pressure pulse arrival, where it remains until 0725 UT (Plate 2c, panel 3).

CME pressure pulse related auroral enhancements are much more global phenomena than isolated substorms, with enhancements of precipitating electron energy flux and latitudinal expansion of both the dayside and nightside aurora. The location of an isolated substorm breakup can be identified within a relatively narrow region in local time, usually near the premidnight or midnight auroral zones (2100-0000 MLT). In contrast, a unique onset location is not observed for auroral intensifications following the arrival of an interplanetary pressure pulse as demonstrated by the August 26, 1998, event.

### 3.2. Average Energies

As with the UVI-derived energy flux, the average energy data are presented in two formats in Plates 1 and 2: MLT-MLAT maps in Apex magnetic coordinates (Plates 1b and 2b) and average energy keograms for various local time sectors (Plates 1c and 2c, even-numbered panels). The time labels on the $E_{ave}$ maps shown in Plates 1b and 2b reference the time of the first image frame used to compute the mean energies, which starts ~ 20 s prior to the images shown in Plates 1a and 2a.

Prior to the onset of the isolated substorm on December 18, 1996, the electron precipitation near local midnight has average energies near 4.1 ± 2.7 keV between 2200-0200 MLT as shown in the 0529:40 UT $E_{ave}$ map (Plate 1b). The hardest electron precipitation at this time is observed in the dusk sector between 1700-1900 MLT with typical $E_{ave}$ values of 10.7 ± 4.2 keV. The electron precipitation near the equatorward boundary of the morning sector oval near 0300 MLT also has higher average energies than in the midnight sector prior to the substorm onset, with $E_{ave}$ values of 6.8

± 3.2 keV. The large errors (≥ 40%) in the inferred $E_{ave}$ values in the 0529:40 UT average energy map are due to the low counts (energy flux less than 3.0 ergs $cm^{-2}$ $s^{-1}$) in the UVI images prior to the substorm onset.

At the onset of the December 18, 1996, substorm (near 0533 UT) the mean energy of the precipitating electrons at the breakup location (between 2300 and 2330 MLT) increases to 14.6 ± 2.6 keV near the equatorward edge of auroral oval (~ 65° MLAT) and 12.2 ± 1.6 keV at higher latitudes near 71° MLAT (Plate 1b, 0532:44 UT $E_{ave}$ map). As the substorm expansion phase ensues after 0535 UT, higher energy electron precipitation with mean energies between 9.8 and 11.3 keV are observed throughout the breakup region between 2200 and 0030 MLT and 65° and 75° MLAT (Plate 1b, 0535:49 UT $E_{ave}$ map). The hardest electron precipitation within the substorm breakup is observed between 2000-2100 MLT near 72° MLAT in the westward surge at the peak of the substorm expansion phase (Plate 1b, 0551:28 UT $E_{ave}$ map). Here the average energy of the electron precipitation is inferred to be 14.3 ± 2.2 keV. This is also shown in the evening sector (2000-2200 MLT) $E_{ave}$ keogram (panel 2), which shows a hardening of the precipitation mean energy to 14.4 ± 2.1 keV near the poleward boundary of the auroral oval between 0541 and 0553 UT when the westward surge of the substorm expansion enters this region. The black-colored pixels within the westward surge region in the 0551:28 UT $E_{ave}$ map are where some average energy values are excluded because they fell outside the range of values for which our analysis is appropriate.

The $E_{ave}$ maps between 0541 and 0603 UT (Plate 1b) show that the precipitating electron average energy is structured in local time and magnetic latitude during the expansion phase of this substorm. In the premidnight sector (2200-0000 MLT), precipitating electron energies are highest near the poleward edge of the substorm expansion while in the postmidnight sector (0000-0200 MLT) the opposite is observed, with the highest $E_{ave}$ values near the equatorward portion of the oval. This pattern is seen between 1800 and 0600 MLT in the average energy maps spanning 0541:57-0603:25 UT (Plate 1b) during the substorm expansion phase. In the premidnight sector (2200-0000 MLT) $E_{ave}$ keogram, both incident electron energy flux and mean energy increase with latitude, indicating that the precipitation within the substorm expansion region hardens as it expands poleward between 0533-0550 UT (Plate 1c, panels 3 and 4). In the dusk sector (1700-1900 MLT) we also observe higher mean energies near the poleward boundary ($E_{ave}$ > 12 keV) than at lower latitudes (Plate 1b). In contrast, the electron precipitation in the postmidnight sector (0000-0200 MLT) has the highest mean energies near the equatorward boundary of the oval. From the substorm onset through the expansion phase, the average energy of electron precipitation is 11.8 ± 3.4 keV near 63° MLAT in the postmidnight region (Plate 1c, panel 6). Similarly, the dawn sector $E_{ave}$ keogram (Plate 1c, panel 8) shows incident electron average energies of 11.9 ± 4.3 keV near the equatorward boundary of the oval (~ 66° MLAT) which decrease with increasing latitude.

Prior to the pressure pulse related auroral intensification on August 26, 1998, the most energetic electron precipitation is seen in the premidnight sector (1900-2100 MLT) where the remnants of a previous intensification are observed until ~ 0653 UT. Here the mean energies of the electron precipitation range between 5.7 and 9.7 keV as shown in the 0650:33 UT $E_{ave}$ map (Plate 2b). The midnight sector (2300-0100 MLT) $E_{ave}$ keogram in Plate 2c (panel 2) shows that the preexisting electron precipitation between 0622 and 0653 UT had a median average energy of 9.2 ± 3.5 keV near the equatorward boundary of the nightside oval (60°-63° MLAT) and 2.8 ± 2.2 keV at higher magnetic latitudes between 66° and 71° MLAT. The electron precipitation in the morningside and dayside ovals, where the aurora is not very dynamic between 0622 and 0653 UT, has $E_{ave}$ values below 6.0 keV (Plate 2c, panels 4 and 6).

Following the pressure pulse arrival, dayside electron precipitation with mean energies between 4.6 and 7.7 keV (Plate 2b, 0653:36 UT $E_{ave}$ map) is observed between 0900 and 1500 MLT. Equatorward of the dayside auroral oval between 1200 and 1800 MLT, where we observed a transient, subauroral enhancement in incident energy flux, the average energy of the electron precipitation is slightly higher than that in the main oval, with $E_{ave}$ values of 5.9 and 8.4 keV (Plate 2b, 0653:36 UT $E_{ave}$ map). During the initial poleward expansion of the dusk sector auroral oval between 1800 and 2100 MLT, average energy values between 10.4 and 12.5 keV are estimated for the precipitation in this broad region (Plate 2b, 0656:40 UT $E_{ave}$ map). This is not reflected strongly in the dusk sector $E_{ave}$ keogram near 0656 UT (panel 8), since the mean energy values shown here are averages over a 2 hour MLT sector. The arrival of the pressure pulse did not significantly affect the electron precipitation near the equatorward boundary of the midnight sector oval. The median average energy in this region after 0653 UT is 12.3 ± 2.0 keV as shown in the $E_{ave}$ maps between 0653:56 and 0656:40 UT (Plate 2b) and the midnight sector $E_{ave}$ keogram (Plate 2c, panel 2).

In comparison to the isolated substorm, the spatial distribution of precipitating electron average energies is less structured at the resolution of the UVI images during this pressure pulse related intensification. The $E_{ave}$ maps in Plate 2b between 0708:56 and 0721:12 UT show that the electron precipitation across the nightside auroral zone between 70° and 80° MLAT and 1800-0600 MLT has average energies between 4.5 and 7.1 keV. Within this region the only structures that appear are two localized patches with slightly higher mean energies between 8.6 and 10.8 keV as shown in the 0708:56 UT $E_{ave}$ map near 72° MLAT just before and after local midnight. These patches are coincident with local-

ized enhancements in the incident energy flux (Plate 2a, 0709:18 UT image). The average energy of the electron precipitation decreases to values ranging between 3.2 and 5.0 keV poleward of 80° MLAT at all local times. The $E_{ave}$ keograms in Plate 2c (even-numbered panels) also show that the electron precipitation following the arrival of the interplanetary pressure pulse was observed at mean energies below 7 keV poleward of 70° MLAT.

During the August 26, 1998, event, in situ measurements of precipitating electrons were made by the Fast Auroral Snapshot (FAST) satellite [*Carlson et al.*, 1998a]. In Figure 1 the UVI-inferred precipitating electron average energies are compared with those measured directly by FAST over the morning sector oval between 0100 and 0200 MLT. The grey line shows the average energy of the downward going electrons (0°-30° pitch angle) between 300 eV and 30 keV as computed from (1). In selecting 300 eV as the lower limit of integration, we have chosen to include mostly plasma sheet electrons in computing the FAST mean energy values shown in Figure 1. The upper integration limit of 30 keV is determined by the highest energy detected by the FAST electrostatic analyzers. The FAST $E_{ave}$ values are averaged over 40 s as shown by the black line in Figure 1. Over this time interval the FAST spacecraft traverses a distance of $\sim$ 200 km near apogee. This is comparable to the size of the MLT-MLAT bins used in the UVI $E_{ave}$ computation. The data points in Figure 1 are the UVI-derived $E_{ave}$ values along the FAST trajectory.

The precipitating electron average energies inferred from UVI are consistent with those measured by FAST, following a similar profile in latitude. However, the UVI $E_{ave}$ values are systematically higher. As FAST moves equatorward from 75° MLAT to 71° MLAT, the average energy of the precipitating electrons it measures gradually increases from $\sim$ 1.5 to 2.5 keV. The UVI-estimated $E_{ave}$ values in this region are higher, increasing from 3.0 $\pm$ 1.9 keV at 74° MLAT to 4.2 $\pm$ 1.3 keV at 71° MLAT. The agreement between the FAST and UVI average energy values improves between 68° and 70° MLAT as both FAST and UVI show the mean energy of the electron precipitation increasing from $\sim$ 5 keV near 70° MLAT to 6 keV at 68° MLAT. The 7.7-keV peak in the mean energy measured by FAST near 65.5° MLAT is not resolved by UVI. Instead, the UVI average energy profile shows a broader peak between 63° and 67° MLAT with a maximum value of 8.6 $\pm$ 1.9 keV. Equatorward of 63° MLAT, the average energies measured by FAST decrease below 4.0 keV. Near the equatorward portion of the FAST trajectory (62° MLAT) the mean energy derived from UVI also decreases with a value of 4.9 $\pm$ 2.1 keV.

In summary, the electron precipitation associated with auroral brightenings is observed to be harder during the isolated substorm than during the auroral intensification immediately following the incident solar wind pressure pulse, particularly during the substorm onset and expansion phase. The regions of the auroral oval with the highest energy flux during the December 18, 1996, isolated substorm are coincident with where the electron precipitation has the highest mean energy ($E_{ave} \geq 10$ keV). In contrast to the isolated substorm, the electron precipitation during the pressure pulse related intensification is softer, with average energies of less than 7.0 keV in the regions where we observe the highest energy flux. The spatial distribution of precipitation electron average energies is ordered in local time

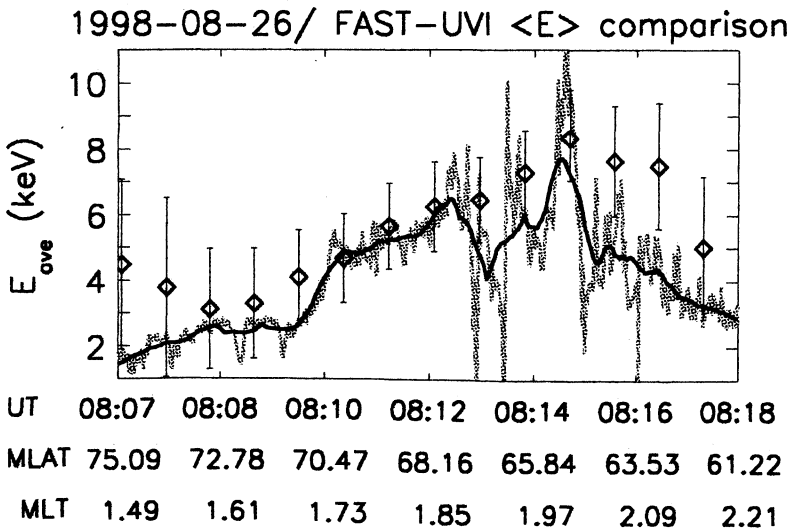


**Figure 1.** A comparison of UVI-derived and Fast Auroral Snapshot (FAST)-derived mean energy values for the August 26, 1998, event. The average energy of the precipitating electrons measured by FAST are shown the by the grey line. A 40-s average of the FAST $E_{ave}$ values is shown by the solid line. The data points (diamonds) are UVI-derived $E_{ave}$ values along the FAST trajectory.

during the isolated substorm while less structure is seen in the $E_{ave}$ maps for the pressure pulse related event for which the mean energy only varied in latitude. A westward surge and the hard electron precipitation associated with it do not appear in the pressure pulse related auroral intensification.

## 4. Discussion

When comparing the FAST and UVI derived mean energies, we find that the UVI $E_{ave}$ values are generally overestimated. We have considered whether the average energy signatures of the two events discussed above, particularly at the substorm onset and immediately following the pressure pulse arrival, are exaggerated by computing LBHl:LBHs ratios from images taken at different times during very dynamic auroral activity. *Germany et al.* [1998] point out that the mean energies derived from the UVI images can be overestimated in situations where the aurora is changing rapidly between two UVI images, especially near boundaries of the auroral oval. However, the aurora is not very dynamic during this period as shown by the UVI keograms in Plate 2c between 0807 and 0818 UT. No significant auroral boundary motions are seen during this period when we compare the FAST and UVI $E_{ave}$ observations.

The discrepancies between the FAST and UVI latitude profiles of $E_{ave}$ values can be accounted for, in part, by the differences in spatial scales over which the $E_{ave}$ values are determined between FAST and UVI. The UVI-derived mean energies are computed over 1.0° MLAT × 0.5 MLT spatial bins while the FAST $E_{ave}$ values are point measurements that only sample a portion of the morning sector oval observed by UVI. Moreover, the scale size of the auroral structures that we can resolve with the coarse spatial resolution of the UVI binned pixels (in MLT-MLAT) is at least 2 orders of magnitude larger than that which can be discerned with the FAST measurements. The UVI average energy estimation is also affected by the wobble of the Polar spacecraft which causes a 1 × 10 pixel smearing in the images. While the MLT-MLAT binning of the UVI images averages out the effects of the wobble, the regions of the images where lower photon fluxes are measured may have larger errors due to the wobble than in brighter portions of the images. Poleward of 71° MLAT where the UVI-derived mean energies are overestimated in comparison to the in situ FAST $E_{ave}$ values (Figure 1), the auroral emissions measured by UVI decrease rapidly with increasing latitude (with an equivalent energy flux below 4.0 ergs $cm^{-2}$ $s^{-1}$) as shown in the midnight sector keogram for this period (Plate 2c, panel 1). Uncertainties in the UVI pointing must also be considered.

The degree to which the FAST and UVI average energy values agree also depends upon the limits of integration one uses when computing the mean energies via (1). However, since the uncertainties in the UVI mean energy estimates are ~ 30% for the data shown in Figure 1, the choice of the minimum energy to use in the FAST $E_{ave}$ computation was not found to have a significant impact on the agreement between the FAST and UVI $E_{ave}$ values for $E_{min}$ between 100 and 500 eV. Moreover, if there was a substantial flux of electrons with energies greater than 30 keV during the period when we are comparing the FAST and UVI mean energy values, the FAST data would give no indication, since these are outside the electron energy range covered by FAST. The precipitation of these greater than 30 keV electrons would, however, contribute to the luminosity measured by UVI and result in an increased estimate for the average energy relative to FAST.

While further comparisons to in situ electron precipitation measurements are needed to increase our confidence in the UVI-derived $E_{ave}$ values during dynamic auroral conditions, previous observations are consistent with the characteristics of the precipitating electrons inferred from the images during the December 18, 1996, isolated substorm. Defense Meteorological Satellite Program (DMSP) measurements of auroral precipitation within a westward surge showed enhanced fluxes of electrons above 20 keV [*Meng et al.*, 1978]. The hardening of the electron precipitation in the westward surge of a substorm has also been reported by *Rème and Bosqued* [1973] from in situ electron measurements obtained by a sounding rocket. They find that the flux of electrons between 5 and 30 keV greatly increased in the westward surge region while electrons fluxes at energies below 5 keV were relatively weak and stable.

The $E_{ave}$ parameter has been interpreted as the average energy that electrons gain from passing through an electrostatic parallel potential [e.g., *Carlson et al.*, 1998b]. Magnetospheric electrons accelerated downward by such potentials constitute regions of upward field-aligned current (FAC). In the postonset mean energy maps for the December 18, 1996, isolated substorm (Plate 1b), the spatial distribution of mean energies near 10 keV and above is consistent with *Iijima and Potemra*'s [1978] statistical pattern of upward field-aligned current for active periods ($|AL| > 100$ $\gamma$). In the dusk and premidnight sectors (1800-0000 MLT) the band of electron precipitation with mean energies above 10 keV lies poleward of 70° MLAT as do the Region 1 upward FAC. In the postmidnight and dawn sectors (0000-0600 MLT) the Region 2 upward field-aligned currents are equatorward of 70° MLAT, which is where we observe the highest mean energy electron precipitation at these local times in the UVI $E_{ave}$ maps. Moreover, the westward traveling surge that we observe in the UVI images during the December 18, 1996, substorm is interpreted to represent the closure of these field-aligned current systems in the ionosphere. This interpretation suggests that the energy characteristics of electron precipitation within the discrete auroral forms observed during substorms are affected by the presence of field-

aligned potential drops which are observed at relatively low altitudes below 2 $R_E$ [*Mozer et al.*, 1977; *Mozer and Kletzing*, 1998].

The hard electron precipitation ($E_{ave} \geq 10$ keV) observed in the postmidnight and dawn sectors of the average energy maps for the December 18, 1996 event, (Plate 1b) is the result of substorm-injected electrons which drift eastward toward the morning side where wave-particle interactions lead to precipitation. The substorm injected electrons with the highest energies arrive first and are detected prior to those with lower energies. This effect is shown by the postmidnight (0000-0200 MLT) and dawn sector mean energy keograms (Plate 1c, panels 6 and 8). Electron precipitation with $E_{ave} > 11$ keV is first observed after the substorm onset near 0533 UT in the postmidnight sector (panel 6). Precipitating electrons with similar mean energies then appear in the dawn sector $E_{ave}$ keogram (panel 8) between 0605 and 0623 UT. The hardening of the electron precipitation in the morningside has been well established by balloon-borne measurements of bremsstrahlung x-rays [*Barcus and Rosenberg*, 1966; *Parks et al.*, 1968].

While the auroral brightening associated with the arrival of an interplanetary pressure pulse has superficial similarities to that observed during substorms, including the poleward excursion of the auroral oval and an increase in the energy flux of electron precipitation, our observations point out key differences in the physical processes during these phenomena. The lower average energy of the electron precipitation observed following an interplanetary pressure pulse arrival and the lack of discrete structure in the $E_{ave}$ maps suggest that the auroral acceleration region is not as important in governing the properties of electron precipitation during these pressure pulse related intensifications. There is no indication of electron injection and subsequent hard morningside precipitation for pressure pulse related auroral activity as there is during substorms. Furthermore, we do not find evidence for the closure of field-aligned currents in the ionosphere via the substorm current wedge (SCW) based on the lack of a westward surge-like feature during the pressure pulse related intensification. This also implies that the processes which may reconfigure the magnetotail are different for isolated substorms and pressure pulse associated intensifications.

The high-energy flux of electron precipitation in dayside local times and in the polar cap not typically observed during isolated substorms raises the question of source populations for the electron precipitation. Although we cannot address this question from the UVI images alone, we can infer that many more regions of the magnetosphere contribute to the pressure pulse related precipitation than during substorms which are typically associated with the plasma sheet in the magnetotail. Examination of in situ observations, such as those made by the FAST satellite, will be necessary to determine if electrons from the high-energy tail of the solar wind distribution are contributing to the high-latitude, polar cap precipitation that is observed during the August 26, 1998, event.

This study has demonstrated the usefulness of auroral imaging in revealing the global aspects of magnetospheric dynamics during auroral substorms and at the initial phase of magnetic storms not possible through satellite point measurements alone. Our results indicate that we must reevaluate the role of interplanetary pressure pulses in triggering auroral substorms. We have shown that the auroral intensifications resulting from the compression of the magnetosphere by a strong solar wind pressure pulse are not auroral substorms in all cases. Auroral substorms represent the injection of magnetotail particles into the near-Earth environment and their subsequent precipitation. In contrast, pressure pulse related auroral activity involves the precipitation of electrons from a larger region of the magnetosphere. Particle simulations will be utilized in future studies to further quantify the different characteristics of substorm versus CME-pressure pulse related electron precipitation.

**Acknowledgments.** The research at the University of Washington is supported in part by NASA grant NAG5-3170.

Janet G. Luhmann thanks John D. Winningham and another referee for their assistance in evaluating this paper.

## References

Akasofu, S. I., The development of the auroral substorm, *Planet. Space Sci.*, *12*, 273, 1964.

Akasofu, S. I., R. H. Eather, and J. N. Bradbury, The absence of the hydrogen emission (H$\beta$) in the westward traveling surge, *Planet. Space Sci.*, *17*, 1409, 1969.

Baker, D. N., T. I. Pulkkinen, X. Li, S. G. Kanekal, J. B. Blake, R. S. Selesnick, M. G. Henderseu, G. D. Reeves, H. E. Spence, and G. Rostoker, Coronal mass ejections, magnetic clouds, and relativistic magnetospheric electron events: ISTP, *J. Geophys. Res.*, *103*, 17,279, 1998.

Bale, S. D., M. J. Reiner, J. L. Bougeret, M. L. Kaiser, S. Krucker, D. E. Larson, and R. P. Lin, The source region of an interplanetary type II radio burst, *Geophys. Res. Lett.*, *26*, 1573, 1999.

Barcus, J. R., and T. J. Rosenberg, Energy spectrum for auroral-zone x-rays, 1, Diurnal and type effects, *J. Geophys. Res.*, *71*, 803, 1966.

Brittnacher, M., M. Fillingim, G. Parks, G. Germany, and J. Spann, Polar cap area and boundary motion during substorms, *J. Geophys. Res.*, *104*, 12,251, 1999.

Brittnacher, M., M. Wilber, M. Fillingim, D. Chua, G. Parks, J. Spann, and G. Germany, Global auroral response to a solar wind pressure pulse, *Adv. Space Res.*, *25*, (7-8), 1377, 2000.

Brueckner, G. E., J.-P. Delaboudiniere, R. A. Howard, S. E. Paswaters, O. C. St. Cyr, R. Schwenn, P. Lamy, G. M. Simnett, B. Thompson, and D. Wang, Geomagnetic storms caused by coronal mass ejections (CMEs): March 1996 through June 1997, *Geophys. Res. Lett.*, *25*, 3019, 1998.

Carlson, C., R. F. Pfaff, and J. G. Watzin, The Fast Auroral Snapshot Mission, *Geophys. Res. Lett.*, *25*, 2013, 1998a.

Carlson, C., et al., FAST observations in the downward au-

roral current region: Energetic upgoing electron beams, parallel potential drops, and ion heating, *Geophys. Res. Lett.*, *25*, 2017, 1998b.

Cogger, L. L., J. S. Murphree, S. Ismail, and C. D. Anger, Characteristics of dayside 5577 Å and 3914 Å aurora, *Geophys. Res. Lett.*, *4*, 413, 1977.

Fox, N. J., M. Peredo, and B. J. Thompson, Cradle to grave tracking of the January 6-11, 1997 Sun-Earth connection event, *Geophys. Res. Lett.*, *25*, 2461, 1998.

Germany, G. A., M. R. Torr, D. G. Torr, and P. G. Richards, Use of FUV auroral emissions as diagnostic indicators, *J. Geophys. Res.*, *99*, 383, 1994a.

Germany, G. A., D. G. Torr, P. G. Richards, M. R. Torr, and S. John, Determination of ionospheric conductivities from FUV auroral emissions, *J. Geophys. Res.*, *99*, 23,297, 1994b.

Germany, G. A., G. K. Parks, M. J. Brittnacher, J. F. Spann, J. Cumnock, D. Lummerzheim, F. Rich, and P. G. Richards, Energy characterization of a dynamic auroral event using GGS UVI images, in *Geospace Mass and Energy Flow: Results From the International Solar-Terrestrial Physics Program*, *Geophys. Monogr. Ser.*, vol. 104, edited by J. Horwitz, D. Gallagher, and B. Peterson, p. 143, AGU, Washington, D. C., 1998.

Gonzales, W. D., and B. T. Tsurutani, Criteria of interplanetary parameters causing intense magnetic storms ($D_{st}$ < -100 nT), *Planet. Space Sci.*, *35*, 1101, 1987.

Iijima, T., and T. A. Potemra, Large-scale characteristics of field-aligned currents associated with substorms, *J. Geophys. Res.*, *83*, 599, 1978.

Kahler, S. W., Solar flares and coronal mass ejections, *Annu. Rev. Astron. Astrophys.*, *30*, 113, 1992.

Li, X., D. N. Baker, D. Larson, R. P. Lin, M. Temerin, T. Cayton, G. D. Reeves, T. Araki, H. J. Singer, and S. G. Kanekai, Energetic electron injections into the inner magnetosphere during the January 10-11, 1997 magnetic cloud event, *Geophys. Res. Lett.*, *25*, 2561, 1998.

Liou, K., P. T. Newell, C. I. Meng, A. T. Y. Lui, M. Brittnacher, and G. Parks, Synoptic auroral distribution: A survey using Polar ultraviolet imagery, *J. Geophys. Res.*, *102*, 27,197, 1997.

Liou, K., P. T. Newell, C. I. Meng, T. Sotirelis, M. Brittnacher, and G. Parks, Source region of 1500 MLT auroral bright spots: Simultaneous Polar UV-images and DMSP particle data, *J. Geophys. Res.*, *104*, 24,587, 1999.

Lummerzheim, D., M. H. Rees, J. D. Craven, and L. A. Frank, Ionospheric conductances derived from DE-1 auroral images, *J. Atmos. Terr. Phys.*, *53*, 281, 1991.

Lummerzheim, D., M. Brittnacher, D. Evans, G. A. Germany, G. K. Parks, M. H. Rees, and J. F. Spann, High time resolution study of the hemispheric energy flux carried by energetic electrons into the ionosphere during the May 19/20, 1996 auroral activity, *Geophys. Res. Lett.*, *24*, 987, 1997.

Meng, C. I., A. L. Snyder, and H. W. Kroehl, Observations of auroral westward traveling surges and electron precipitation, *J. Geophys. Res.*, *83*, 575, 1978.

Mozer, F. S., and C. A. Kletzing, Direct observations of large, quasi-static, parallel electric fields in the auroral acceleration region, *Geophys. Res. Lett.*, *25*, 1629, 1998.

Mozer, F. S., C. W. Carlson, M. K. Hudson, R. B. Tolbert, B. Parady, J. Yatteau, and M. C. Kelley, Observations of paired electrostatic shocks in the polar magnetosphere, *Phys. Rev. Lett.*, *38*, 292, 1977.

Parks, G. K., F. V. Coroniti, R. L. McPherron, and K. A. Anderson, Characteristics of modulated energetic electron precipitation occurring during auroral substorms, *J. Geophys. Res.*, *73*, 1685, 1968.

Rème, H., and J. M. Bosqued, Rocket observations of electron precipitation in a westward-traveling surge, *J. Geophys. Res.*, *78*, 5553, 1973.

Rees, M. H., and D. Lummerzheim, Characteristics of auroral electron precipitation derived from optical spectroscopy, *J. Geophys. Res.*, *94*, 6799, 1989.

Richmond, A. D., Ionospheric electrodynamics using magnetic apex coordinates, *J. Geomagn. Geoelectr.*, *47*, 191, 1995.

Spann, J. F., M. Brittnacher, R. Elsen, G. K. Parks, and G. A. Germany, Initial response and complex polar cap structures of the aurora in response to the January 10, 1997 magnetic cloud, *Geophys. Res. Lett.*, *25*, 2577, 1998.

Strickland, D. J., J. R. Jasperse, and J. A. Whalen, Dependence of auroral FUV emissions on the incident electron spectrum and neutral atmosphere, *J. Geophys. Res.*, *88*, 8051, 1983.

Strickland, D. J., R. R. Meier, J. H. Hecht, and A. B. Christensen, Deducing composition and incident electron spectra from ground-based auroral optical measurements: Theory and model results, *J. Geophys. Res.*, *94*, 13,527, 1989.

Torr, M. R., et al., A far ultraviolet imager for the International Solar-Terrestrial Physics mission, *Space Sci. Rev.*, *71*, 329, 1995.

Zhou, X., and B. T. Tsururani, Rapid intensification and propagation of the dayside aurora: Large scale interplanetary pressure pulses (fast shocks), *Geophys. Res. Lett.*, *26*, 1097, 1999a.

Zhou, X., and B. T. Tsurutani, A new mechanism for substorm triggering during interplanetary shock compression events, *Eos Trans. AGU*, *80*(46), Fall Meet. Suppl., F885, 1999b.

M. Brittnacher, D. Chua, G. Parks, and W. Peria, Geophysics Program, Box 351650, University of Washington, Seattle, WA 98195. (damien@geophys.washington.edu)

C. Carlson, Space Sciences Laboratory, University of California, Berkeley, CA, 94720.

G. Germany, CSPAR, University of Alabama in Huntsville, Huntsville, AL 35899.

J. Spann, NASA Headquarters, Washington, D. C., 20546.

(Received May 3, 2000; revised August 2, 2000; accepted August 2, 2000.)